Multi-Window Setup for Thermomechanical Experiments Assisted by DIC up to 900°C

Rafael Vargas[a,b] ⓘ, *Igor Paganotto Zago[a]* ⓘ, *Vinicius Fiocco Sciuti[c]* ⓘ, *Matheus Furlan[a]* ⓘ,

Ricardo Afonso Angélico[d] ⓘ, *François Hild[b]* ⓘ, *Rodrigo Bresciani Canto[a,c]* ⓘ

[a]*Universidade Federal de São Carlos, Programa de Pós-Graduação em Ciência e Engenharia de Materiais (PPGCEM), São Carlos, SP, Brasil.*
[b]*Université Paris-Saclay, CentraleSupélec, École Normale Supérieure Paris-Saclay, Centre National de la Recherhe Scientifique (CNRS), Laboratoire de Mécanique Paris-Saclay (LMPS), Gif-sur-Yvette, France.*
[c]*Universidade Federal de São Carlos, Departamento de Engenharia de Materiais Engineering (DEMa), Rod. Washington Luiz, km 235, São Carlos, SP, Brasil.*
[d]*Universidade de São Paulo, Escola de Engenharia de São Carlos, Departamento de Engenharia Aeronáutica, Av. João Dagnone, 1100, Santa Angelina, São Carlos, SP, Brasil.*

Mechanical properties may drastically change with temperature, which is crucial to characterize materials in environments as similar as possible to their desired application. This paper discusses a new furnace designed for thermomechanical experiments assisted by Digital Image Correlation (DIC) up to 900°C, with six transparent windows that allow for the visualization and lighting of the specimen. Its versatility is demonstrated in three different experimental configurations, namely, dilatometry, three-point bend experiment, and wedge splitting test. Applied forces and full-field data are used for robust calibration of parameters for numerical simulations.

Keywords: *Experimental development, full-field measurements, high temperature, refractories, multiview system.*

1. Introduction

Uncountable products and services rely on materials under high-temperature in-service conditions, ranging from some degrees above room-temperature up to over 2000°C. For applications related to transportation, polymeric matrix composites with carbon fibers present good specific thermomechanical properties that can be further improved when fillers are used[1]. High-performance polymers, such as polytetrafluoroethylene (PTFE), have a melting temperature of the order of 320°C, while chemically inert to many solvents and with high electrical resistivity that make them useful for a wide range of applications among which gaskets or cable insulation in hazardous environments[2]. Another polymer, polyether ether ketone (PEEK), may take years to degrade up to 350°C, especially under inert atmospheres[3]. Metals and ceramics applications may reach even higher temperatures, sometimes above 1000°C, as in aircraft engines[4] or inside nuclear reactors for energy production[5,6]. A wide range of composite systems has also been developed to operate under high-temperature conditions[4,7]. Their thermomechanical behavior is also a topic of interest[8,9]. As the application temperature increases, for instance aiming to increase the energetic efficiency, risks and costs increase and more knowledge about the materials at these conditions is required for an effective and secure design of structures.

There are numerous challenges in assessing mechanical properties at high temperatures, in particular above some

hundreds of Celsius degrees[10]. Some common measurement devices such as strain gauges and clip gauges are not practical or feasible to be used in these environments, and indirect measurements (*e.g.,* actuator displacement) are usually strongly influenced by the setup flexibility and temperature gradients. One alternative to this scenario is using Digital Image Correlation (DIC)[11-13]. DIC is a high-resolution and full-field measurement technique whose main advantage over conventional extensometry in this context is not requiring physical contact with the specimen. Moreover, it mitigates the need to install sensors that withstand high temperatures and have wiring outside of the heating chamber. Further, full-field measurement results are desirable to identify material parameters and validate constitutive models[14-19].

Image-based techniques for high temperature tests are also challenging due to heat haze effects and black-body radiations[10,11,20,21], which may bias the analyses. Speckle patterns may also change with temperature[22,23], thereby calling for regularization strategies in DIC analyses. Last, the study of quasi-brittle refractories deals with small strains that may be lower than intrinsic uncertainties of some experimental setups. Recently, considerable effort has been made to develop setups for investigating the thermomechanical behavior of ceramics assisted by full-field measurements using images. For instance, heating the surface with a laser before applying mechanical load (while capturing images) is one approach successfully used to investigate damage in ceramic-ceramic composites (CMCs)[21,24,25]. Such technique

*e-mail: r.vargas_m@hotmail.com

is ideal for small samples but cannot produce homogeneous temperature variation in bigger samples.

Another interesting alternative is using heating and loading systems coupled with laboratory tomographs[26] or synchroton beamlines[27-30] for acquiring X-ray images during thermomechanical loadings. The images are used to reconstruct volumes that are then analyzed with Digital Volume Correlation (DVC), the volumetric counterpart of DIC. All the cited references for DVC analyses dealt with CMC samples in the range of few millimeters in size to achieve fine resolutions during tomography. A different approach is using testing systems in which a furnace with a transparent window allows for specimen visualization and DIC analyses. For example, tensile tests were used to investigate creep at 900°C for a woven CMC, which were also analyzed with a priori and post-mortem tomographies[31]. Bending tests were run for checking asymmetry (*e.g.,* shift in the neutral line position) in an aluminum titanate sample at 900°C[32], and they were used to identify elastic and fracture properties of ZrO_2-doped $YTaO_4$ ceramics at 800°C[33]. Brazilian (*i.e.,* diametral compression) tests performed at 900°C were analyzed using analytical equations for obtaining the Young's modulus and tensile strength of ion transport membranes[34]. A similar test was performed up to 1200°C to investigate optimal speckle pattern for measuring strains and crack lengths via DIC for an alumina-spinel refractory[35]. Last, wedge splitting tests (WSTs) at 25°C, 800°C, and 1200°C were conducted for calibrating fracture and cohesive parameters of an industrial refractory by inverse analyses exploiting the forces and crack lengths[36].

This paper aims to overcome some of challenges induced by high temperatures when designing a new furnace for performing thermomechanical tests assisted by DIC up to 900°C. The applied guidelines are provided to help readers who may be interested in building similar setups for obtaining measurements that are not possible with other methodologies. The setup is first described, emphasizing practical aspects. The experimental choices for reducing DIC uncertainties are also discussed. Further, having six transparent windows, enabling for different viewing angles in the sample, is another innovative aspect of the setup. This configuration allows full-field data to be extracted from different sides of the specimen, which is useful for capturing 3D effects in mechanical tests[37,38] and compensating for out-of-plane motions[39,40]. Then, the potential application of such a furnace is exemplified with three experiments, namely, dilatometry, three-point bending, and WST for which thermomechanical parameters are calibrated.

2. F900 Project

The instrumented furnace presented in this paper (designated as F900) was designed to be coupled to a universal testing machine (UTM) MTS Exceed E44.304 (30 kN capacity). The design and construction of this equipment are challenging due to the features that enable for the application of the DIC technique. This section details such features, providing design solutions to overcome these intrinsic challenges. As will be shown in the results section, the F900 furnace allows for enhancing experimental tests by extracting more data and new information from a single test (via full-field data), unreachable using conventional measurement sensors such as extensometers or LVDTs. Details provided herein

are helpful to conduct experiments assisted by DIC at high temperatures. The methodological development of new characterization techniques, which are more adapted to study materials close to their in-service conditions, aims to aid the understanding of material behavior and, thus, increase the possibilities to improve processing, formulation, and microstructures.

The F900 design had a dimension constraint of 400 mm between the columns of the testing machine, represented in the top view of the furnace configuration in Figure 1. The furnace inner cavity width was limited by the required refractory wall thickness to insulate the testing machine columns and avoid its overheating. The overall internal cavity dimensions are 280 mm in height, 170 mm in width and 210 mm in depth to position specimens and loading devices. Two sliding doors are used to close the furnace, and each one is equipped with three transparent inspection windows, a bigger one in the center and two smaller ones at 30° angle from the former. Their respective view ports are 110 mm and 50 mm in diameter. The windows comprise two layers of quartz glass, spaced by an alumina tube (50 mm in length) for insulation purposes. It is important to note that this multi-window setup can be used in different configurations, both for lighting and image capture, making it possible to apply stereocorrelation[12]. All the images acquired for the present discussion were gathered through the bigger windows, while blue LEDs were positioned on the other ones.

The furnace project was designed using Inventor™ CAD software. The main features are highlighted in Figure 2. Two controllers are used to have two temperature-controlled zones (operating independently) along the vertical direction. This design choice tends to decrease the vertical gradient of the temperature field. Two or more thermocouples and an independent acquisition system is used to record the temperature of the experiments conducted in the F900 furnace. Another
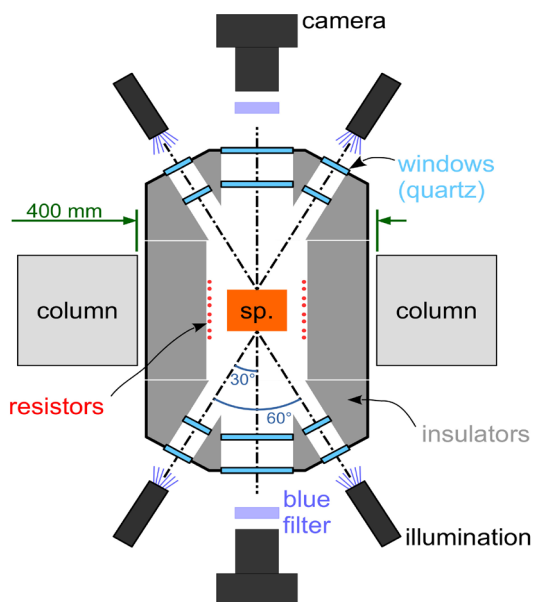
Figure 1. Top view of the furnace for up to 900°C tests displaying the setup used in the analyses presented in Section 3.

design requirement was the mounting and dismounting from the testing machine since it is possible to carry out experiments without controlled mechanical loading (*e.g.,* dilatometry or creep tests with dead load). In order to perform such tests, a U-beam with rails is used for easier alignment of the cameras, furnace windows, and samples.

A modular approach was designed for positioning the whole setup with detachable parts, which is shown in Figure 3(a). For instance, the only non-movable part is the central zone of the furnace, which is fixed in the center of the U-beam over four guiding pins to ensure alignment with the lower actuator. Moreover, the doors are attached over guiding pins, but on gliding supports that allow the furnace to be easily opened and closed by sliding the doors. Similarly, the supports for the cameras and lighting are attached on the

rails to maintain the alignment and for easy adjustment of the distances from sample surfaces. An image of a heated WST sample inside the setup is shown in Figure 3(b). All this setup was mounted over a workbench with adjustable height, which could also be used for easier alignment of cameras on other mechanical experiments without the furnace.

2.1. Active cooling systems

A system made of aluminum sheets and small fans was designed and attached in the 20 mm gap between the furnace and the UTM columns (at each side) to avoid overheating (see "lateral cooling" in Figure 2). This solution allows the lateral column temperature to be less than 50°C while not removing too much heat from the furnace laterals, which would demand more energy to control the furnace inner
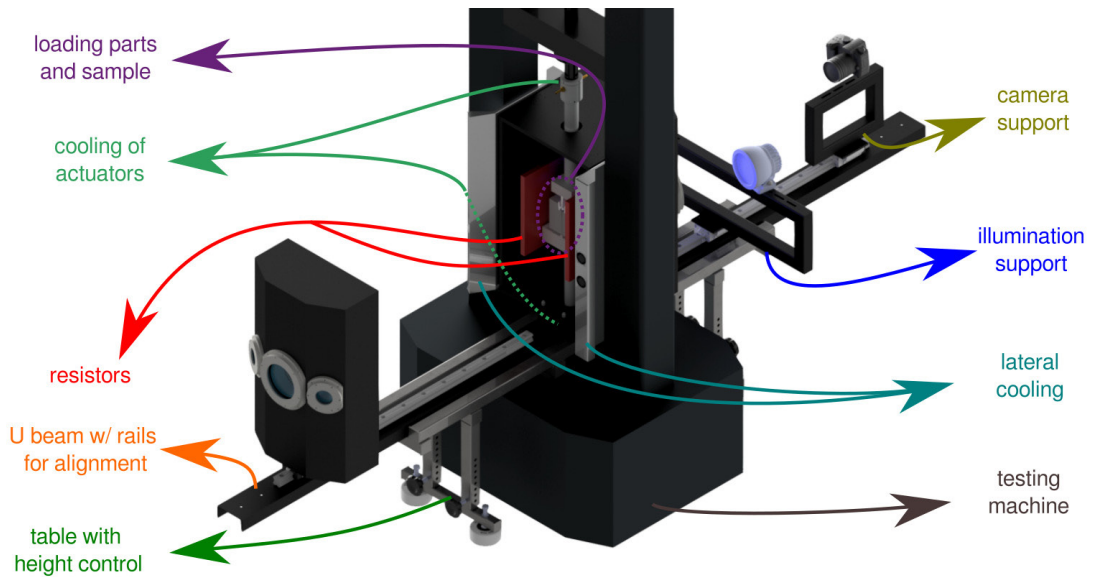

Figure 2. 3D assembly of the developed F900 setup to perform thermomechanical experiments up to 900°C.
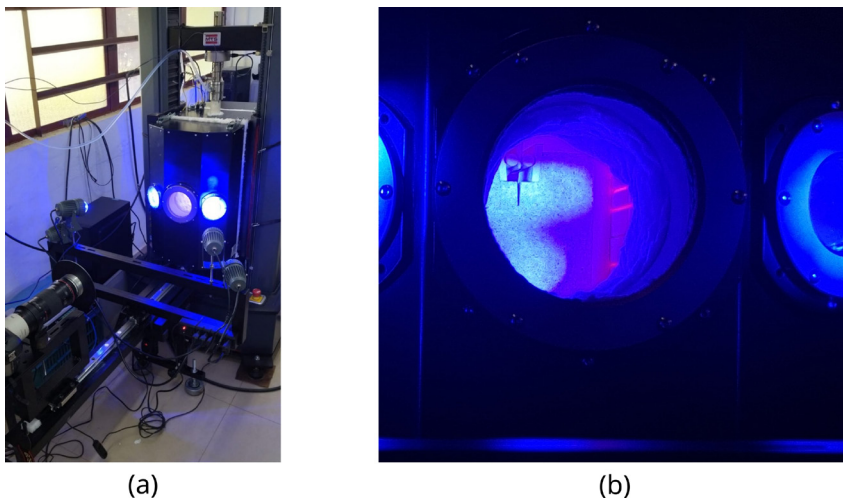

**Figure 3.** (a) Finalized F900 setup, with (b) a zoom on a WST specimen at 900°C.

Figure 4. (a) CAD project of the coupling/cooling parts for the actuators and (b) the final parts in stainless steel. See "cooling of actuators" in Figure 2 for visualizing these parts in the setup.

temperature. Preliminary thermal analyses in Finite Element (FE) commercial codes indicated that the external part of the actuators could reach up to 300°C if no cooling was utilized. Therefore, another cooling part was designed to be coupled at the outer end of each actuator, with inner channels (see Figure 4(a)) connected to a water pump whose aim is to remove heat near the load cell to an external reservoir, keeping its temperature less than 40°C (the maximum working temperature given by the manufacturer). Actuators with diameters up to 50 mm can be fixed with three lateral screws 120° from each other after proper contact and alignment between the actuator and cooled coupling faces. Even if the current actuators are not screwed in the cooling parts, actuators could also be made with some metallic nickel-based superalloys, which make grinding (for setting both surfaces parallel) easier than with ceramic parts. This solution would allow other setups than those discussed in this paper to be easily coupled, further increasing the versatility of the F900 furnace. Both produced parts in stainless steel are shown in Figure 4(b).

2.2. Loading and test accessories

To perform thermomechanical experiments at 900°C, the actuators need to resist loading at this temperature and also sustain a thermal gradient from 900°C inside the furnace to almost room temperature at the outer end. The actuators are 300 mm in length and have diameters of about 45 mm, thereby resulting in compressive stresses of the order of 20 MPa under the maximum loading capacity of the testing machine (30 kN), which is deemed low for several refractories. The actuators were made of refractory mortar, using a polyvinyl chloride pipe as mold with a machined polyethylene cap at the bottom. The top actuator had a small reduction in diameter ground some millimeters away from one flat end to attach it to the moving part (*i.e.,* the three screws 120° apart, see Figure 4(a)) of the testing machine to apply load.

Along with the actuators, other loading parts are required for experiments at high temperatures. In this work, the setups designed for classical bend tests and WSTs are discussed, as illustrated in Figure 5. For the bend tests (Figure 5(a)), they were designed in a way to have inclined grooves to fit the
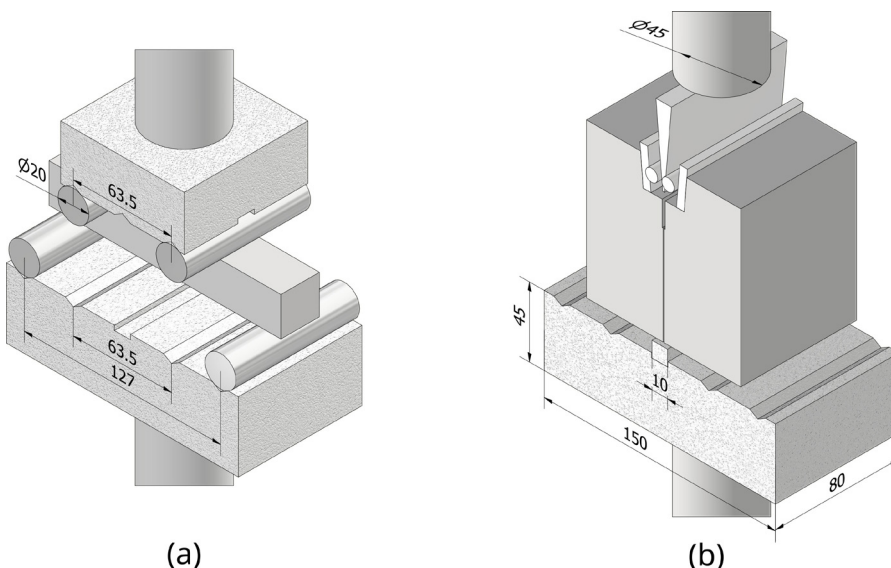
Figure 5. 900°C setups for (a) bend experiments and (b) WSTs. Dimensions are given in mm.

cylinders for applying the load in three-point or four-point configurations. The same bottom part has another groove in the middle to fit the parallelepipedic support for WST samples (Figure 5(b)). These parts were manufactured using refractory mortar and 3D-printed counter-molds. The bottom part, 150 mm in width, helps the sample to be held after fracture, lowering the risk of damaging the heating elements of the furnace.

## 2.3. Camera lenses, filters, and illumination

There are some challenges for image-based techniques on high temperature setups. Heat haze and black-body radiation may compromise the hypothesis of straight ray paths and gray level conservation. For instance, at 900°C, materials emit visible red radiations that may saturate the red channel of a camera and reduce contrast. To mitigate these effects, a series of filters was used. A system was machined in aluminum alloy to attach different lenses in front of the original camera lens. From the furnace to the camera there are near-IR hot mirrors, which are used to protect the camera by reflecting infrared wavelengths between 750 and 1200 nm (FM201 from Thorlabs). Blue bandpass filters with a bandwidth ranging from 360 to 580 nm (FGB39S from Thorlabs), shown in Figure 6(a), were used to reduce the effect of black-body radiation, avoiding the acquisition of the strong red light emitted by the heated sample. After testing different types of illumination, 10-W blue LEDs with 800 lumens were chosen, see Figure 6(b). The filters provided stable results with a high dynamic range (*i.e.,* difference between maximum and minimum gray levels) and small oscillations in the blue channel when comparing images acquired at different temperatures. Their mounting on the spotlight geometry with a narrow beam aligned by its glass lens helped maintain a constant and strong illumination on the specimen surfaces, surpassing the light radiated by the sample. A total of eight LEDs was used per experiment, two at each window, mounted in an illumination support (Figure 2) to allow for easier positioning by adjusting their distance from the furnace doors and height of the spots depending on the specimen geometry.

Canon 5DS cameras were used. Their raw file has three color channels, namely, red, green and blue hues. The blue channel was chosen for all the analyses reported in this paper due to the blue filter and blue LEDs mentioned before, which reduce the capture of varying red light caused by black-body radiation. This choice contributes to ensuring the hypothesis of gray level conservation used in DIC[41]. Further, to deal with heat haze during tests, which changes the refraction index of the heated air in motion due to convection, a long time (*i.e.,* above one second) averages the optical flux intensities mitigating such effects[42]. It also increases the light intensity, which may saturate images.

To overcome this side effect, neutral density filters (one ND2000 from Rise(UK) and one variable ND2-ND400 from K&F Concept) were used to reduce the overall brightness and keep a good contrast, thereby helping to reduce the uncertainty in DIC analyses[42].

2.4. Patterning procedure for high temperatures

DIC results are greatly affected by the random pattern of gray levels of the specimen surface. If the specimen does not have a natural pattern that can be used, usually, an artificial texture is applied to the specimen surface. Conventional inks do not withstand high temperatures and contrast may change or be lost during experiments. After testing different strategies, the most practical and effective path for the presented analyses was the use of a ceramic slurry sprinkled onto the specimen surfaces using a paint-brush. Conventional high-temperature spray inks were tested, resulting in complete disappearance of the artificial contrast. The silicon carbide slurry used for patterning had a small color change when first heated to elevated temperatures. After first heating, it did not change. Therefore, the dilatometry experiments were executed in specimens that had already been heated up to 900°C for pattern stabilization purposes. For the isothermal thermomechanical experiments, a temperature stabilization time of few hours ensured for pattern consistency throughout the experiments. Figure 7 illustrates the change in contrast for a WST sample patterned with the silicon carbide slurry before and after first heating.
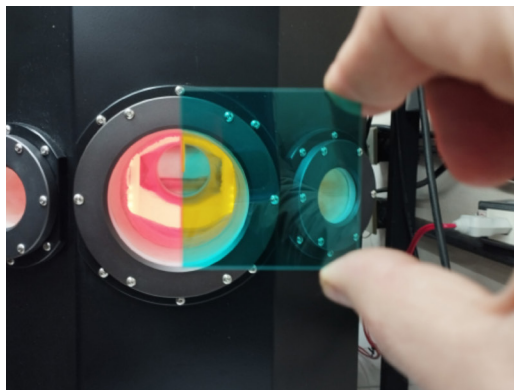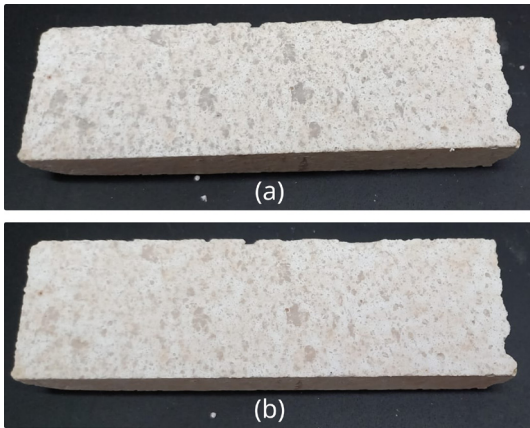

Figure 6. (a) Effect of the blue bandpass filter on image acquisition at 900°C. (b) 10W blue LED illumination dedicated to one of the furnace windows.

Figure 7. Silicon carbide slurry pattern of a parallelepipedic sample (of approximately $10 \times 25 \times 120$ mm³) made of the same material used in three-point bending (Section 3.2) and WST (Section 3.3) (a) before and (b) after being heated up to 900°C.

3. Examples of Application

In this section, three tests performed using the F900 furnace are reported. First, a dilatometry experiment was performed using the furnace and the alignment setup (*i.e.,* rails and supports) outside the testing machine. Then, two thermomechanical experiments are presented, namely, three-point bending (TPB) and one WST. All the experiments are presented with a simplified analysis to illustrate the use of full-field data and highlight its potential applications, with measurements that may not be achievable in usual setups. The DIC hardware parameters for the three discussed experiments are gathered in Appendix A.

3.1. Dilatometry test

The F900 furnace along with DIC can be used to study dilatometry experiments. Contrary to conventional push-rod dilatometry, specimens of different sizes and geometry can be tested. Being a non-contact measurement technique, materials that oxidize are less problematic. Expansion anisotropy (and even localized anisotropy) can be measured in a single experiment and defects that may appear in the material can be detected. The push-rod may compress materials that lose their rigidity with the rise of temperature and induce biased results. In F900, the material is only affected by its own weight in DIC-monitored dilatometry.

An Yttria Stabilized Zirconia (YSZ) specimen, produced with 3 mol% of yttria, with spray-dried particles with a maximum size of 50 μm was used for the reported dilatometry experiment. The specimen was prepared by uniaxial pressing at 40 kN (*i.e.,* about 28 MPa). Then, the green compact was sintered at 1450°C, resulting in a geometry of $9 \times 54 \times 15$ mm³ and a mass of approximately 40 g. The linear specimen shrinkage after sintering was about 22%.

The specimen was patterned with a silicon carbide slurry. The dilatometry analysis was carried out in the F900 furnace while acquiring images from two opposite sample faces. The cameras were positioned at the same working distance from each opposite monitored surface. This procedure allows the use of the average thermal strain between both analyzed faces, compensating for out-of-plane rigid motions. This strategy was possible thanks to the ability of visualizing two opposite faces, which enabled the Coefficient of Thermal Expansion (CTE) to be evaluated for the YSZ specimen. The temperature acquisition was obtained with a thermocouple close to the specimen. The experiment was performed with an image acquisition rate of one frame per minute and a heating rate of 2°C/min. The initial temperature was set to 50°C, and the experiment was carried out as a single ramp until the control system reached 850°C, when a dwell was kept for 30 min, before ending the experiment.

A blue rectangle delimits the specimen positioned over a flat surface in Figure 8(a,b), with the larger faces of the specimen facing each camera. A rectangular mesh with three-noded linear triangular elements (T3) with a mean size of 2.4 mm (or 179 px) was used to quantify the expansion of the YSZ specimen. The horizontal and vertical displacement fields, after removal of rigid body motions, are shown in Figure 8(c,d) and 8(e,f), respectively, for the maximum temperature of the experiment (850°C) where the displacement magnitude is less than 200 μm. The displacement uncertainties were evaluated with twenty reference images before heating started (Apendix A) and was on average equal to 5 cpx (*i.e.,* ≈ 0.7 μm).

The differential or tangent CTE α is calculated using the strain increment $d\overline{\epsilon}^{th}$ from an infinitesimal temperature variation dT

$$\alpha = \frac{d\overline{\epsilon}^{th}}{dT} \tag{1}$$

The CTE of YZS was obtained by evaluating the mean thermal strain variation, $d\overline{\epsilon}^{th}$, which was considered as the average of the maximum and minimum eigenstrains for all the elements in the mesh as a function of the temperature variation. In the present case, the standard uncertainty of $d\overline{\epsilon}^{th}$ was equal to 2.5×10^{-4}. The thermal strains measured for each camera, and the corresponding average (with its standard deviation) are presented in Figure 9(a). The CTE values from each camera or considering their average are compared in Figure 9(b) to the results reported by Hayashi et al.[43], where the CTE of YSZ with different concentrations of yttria from -173 to 627°C were evaluated via push-rod dilatometry. Despite differences of $\pm 1 \times 10^{-6}$°C⁻¹ in CTE values measured using the average result and by Hayashi et al.[43] (Figure 9(b)), the slopes are virtually the same. The results considering both cameras separately led to different slopes. The difference in the comparison with Ref.[43] may be explained by minor differences in yttria content.

The 3% YZS material results from Hayashi et al.[43] were chosen based on similar composition as the material studied herein. No other studies were found reporting CTEs for this composition. The authors evaluated different contents of yttria (3, 6, 8 and 10%) and their effect on the thermal expansion of YZS, concluding that the increase of yttria reduced the material thermal expansion. No uncertainty was reported when reporting the measurements. Thus, it does not allow for a direct comparison to the measurements presented in Figure 9.
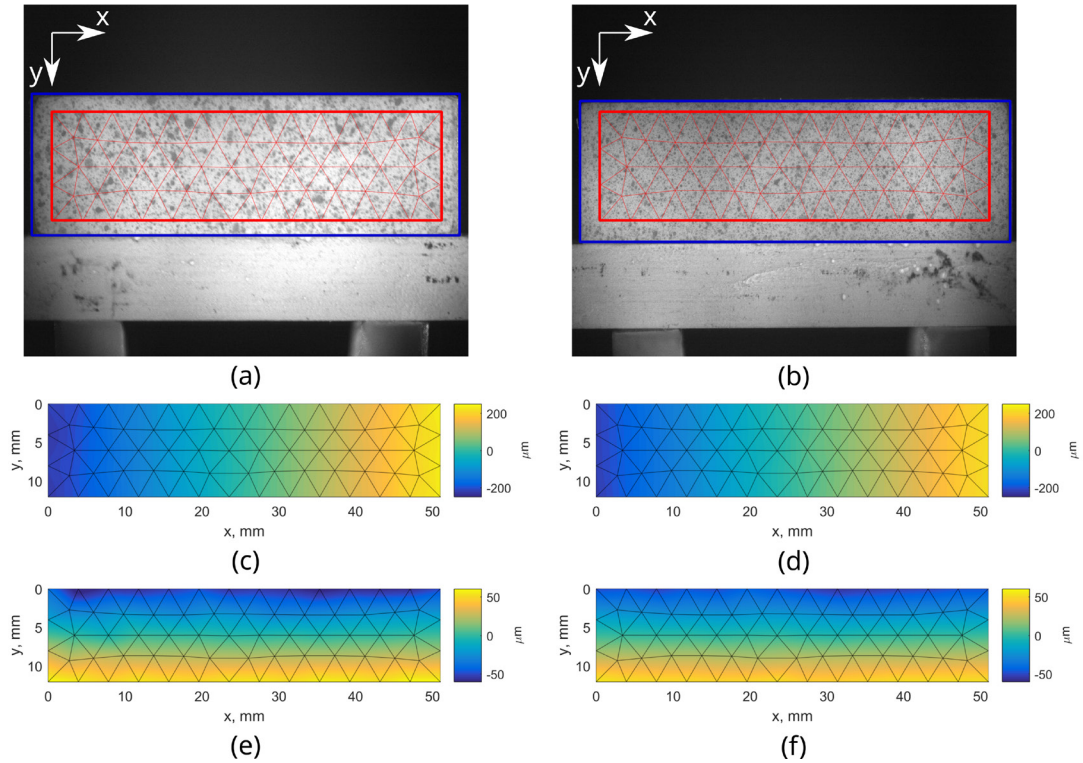
Figure 8. (a,b) References images with the meshes (in red) used for analyzing the YSZ specimen dilatometry up to 850°C. (c,d) Horizontal and (e,f) vertical displacement fields for the maximum temperature. Sub-figures for the front face in (a,c,e) and for the back face in (b,d,f). In the images, 1 px ≈ 13.4 µm.
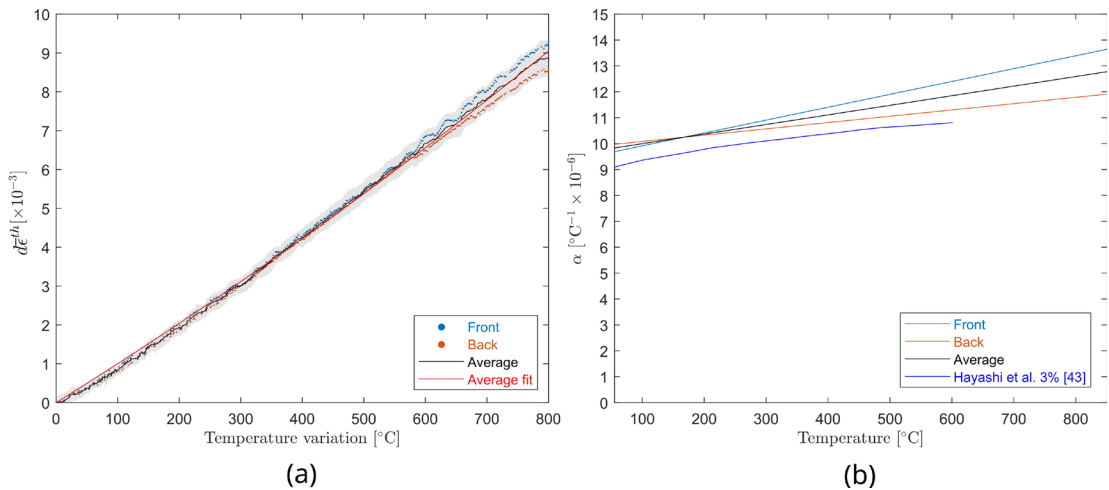
Figure 9. Dilatometry test conducted in the F900 furnace for a YZS specimen. (a) Thermal strain computed for DIC results with images of the two opposite faces of the specimen and its average value. A second-degree polynomial interpolates the thermal strain average to allow for the computation of the differential CTE. The gray patch shows the standard strain uncertainties. (b) Differential CTE α obtained from the DIC analyses of opposite sides of the specimen. The average of them is compared with literature results[43].

Other literature data on the thermal expansion of YZS with higher yttria content may also be compared with those of Hayashi et al.[43], for instance, Kulczyk-Malecka et al.[44] used a thermomechanical analyzer (Setsys Evolution 16118 – Setaram) to evaluate the CTE of a 7% yttria YZS, and Dey et al.[45] a NETZSCH - DIL 402 C push-rod dilatometer to evaluate the CTE of an 8% yttria YZS. The results shown herein and the aforementioned references all overestimate the CTE levels presented by Hayashi et al.[43].

Observing the assessed thermal strain (Figure 9(a)) and CTE results (Figure 9(b)) illustrates the importance of obtaining data from both opposite sides of the sample to mitigate the effect of out-of-plane motions. This setup allows dilatometry tests to be performed for materials unsuitable for usual dilatometry setups (*e.g.,* with big aggregates in the composition), or to evaluate localized phenomena due to thermal loadings such as phase transformations and/or cracks. For further validating this methodology, a comparison of this methodology with a push-rod dilatometer results in a calcined alumina sample is presented in Appendix B.
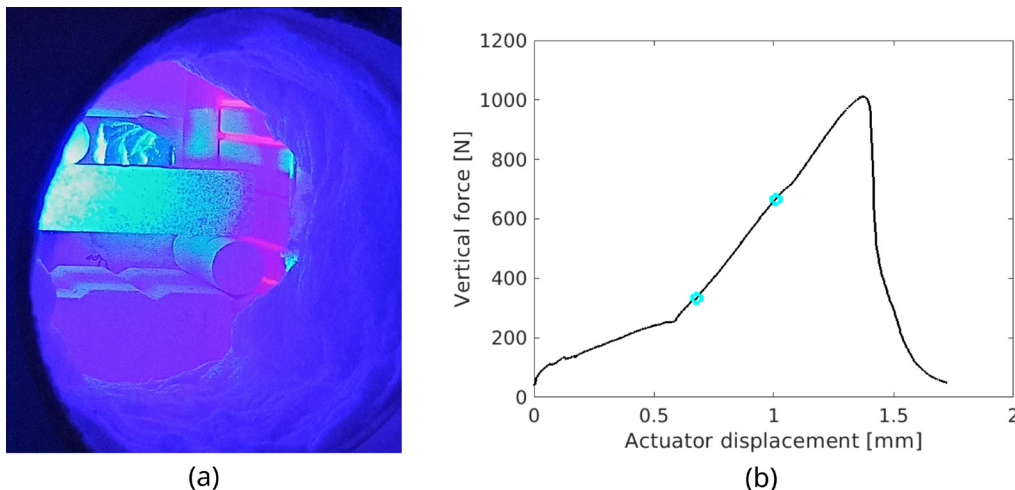
3.2. 3-point bend experiment

A sample of size $150 \times 25 \times 25$ mm^3, which illustrates the use of bend tests, is shown inside the F900 setup at 900°C in Figure 10(a). This sample was made of an alumina castable refractory with mullite-zirconia aggregates, which was sintered at 1400°C, and was also used in preliminary dilatometry and pattern analyses. More information about the material and analogous sample processing is found in Refs.[46,47]. Heating was performed at 10°C/min, and a dwell of 1.5 h was applied at 900°C to ensure thermal stabilization of the whole furnace. During heating, the testing machine was controlled to keep the applied force between 40 N and 50 N. Ten reference images were acquired after reaching a pre-load of 50 N. The loading started at a rate of 20 μm/min, and the resulting loading curve is shown in Figure 10(b), where accommodation with a smaller slope up to 0.6 mm of actuator displacement is observed before a linear regime. Some post-peak softening also occurred, even after considerable force drop from the ultimate load.

Reference images for both sides are displayed in Figure 11(a,b), together with a blue contour highlighting the sample positioning and regions of interest for DIC analyses. The mesh with a mean element size of 1.2 mm (or 80 px) was considered in a larger area avoiding the outer shadows for checking the overall kinematics, while the cyan circles depict the force application points of the three cylinders. The applied pattern is visible, providing sufficient contrast

for DIC measurement purposes. Both horizontal displacement fields (after removing rigid body motions) for the ultimate load are displayed in Figure 11(c,d) showing extension at the bottom part and contraction at the top (as expected). Even at the maximum load, the displacement amplitude remained of the order of 50 μm, thereby illustrating the importance of optimizing the experimental setup and having a robust DIC code to achieve low measurement uncertainty. For the reported experiment and DIC mesh, the standard uncertainty is equal to 5 cpx (or 0.7 μm), which was calculated as the standard deviation among the ten reference images taken at 900°C prior to starting the mechanical loading (Appendix A). The displacement fields are also shown for the last analyzed frame in Figure 11(e,f), where the displacement jump is considerably more pronounced since a crack had already propagated through most of the specimen height.

To calculate the Young's modulus of the tested material, Euler-Bernoulli beam kinematics was used[48]. Two beam elements are needed in the present case, whose nodes are horizontally positioned at the load application points (cyan circles in Figure 11(a,b)). It is worth noting that in the present case, two of them were not visible since they were hidden by the insulators near the transparent windows. Although some improvements can be made to increase the ROI for bend tests, it is worth noting that the distance between the bottom supports was 127 mm, while the central visualization windows have a 110 mm diameter. However, the modular aspect of the oven doors allows, if needed in the future, for an attachable door with horizontal windows better suited for bend tests to be constructed. Thus, with this limited ROI, such an approach integrating analytical equations to describe the kinematics (also called Integrated-DIC[49]) enables for trustworthy results, while avoiding the need for post-processing displacement fields and diminishing possible uncertainty propagation.

In the present case, there are 9 degrees of freedom to be determined, namely, 6 translations and 3 rotations at each element end. By construction, with the selected shape functions, the displacement and rotation fields are continuous.

(a)   (b)

Figure 10. (a) Three-point bending sample inside the F900 furnace at 900°C during the experiment. (b) Resulting loading curve. The cyan circles depict the region where the Young's modulus was calculated.
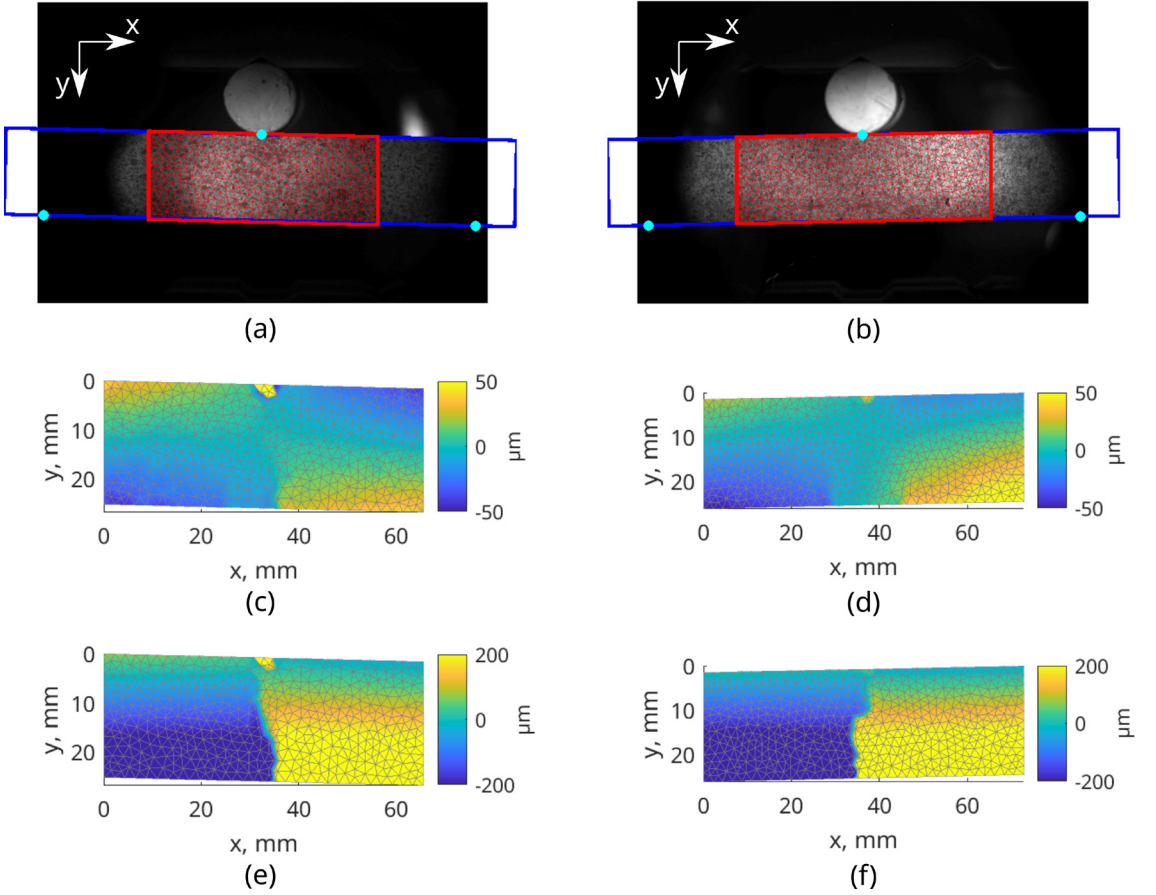
Figure 11. (a,b) References images with the meshes used for analyzing the three-point bend test performed at 900°C. The blue contour delineates the specimen, the red contours depict the mesh used for analyzing the more illuminated region on both sides, and the cyan circles depict the contact points of the sample with the cylinders. Horizontal displacement fields for (c,d) the time step with the maximum force and (e,f) for the last analyzed time step. Results for the front face in sub-figures (a,c,e) and for the back face in sub-figures (b,d,f). 1 px ≈ 14.8 μm.

Further constraints were added (via 5 Lagrange multipliers), namely, continuity of the curvature, no bending moment (*i.e.,* zero curvature) at both ends of the beam, no global extension/contraction of the beam. With such hypotheses, there were only 4 degrees of freedom, namely, the three rigid body motions and the beam deflection. With such reduced kinematics, the noise influence is reduced and a more robust estimate of the Young's modulus, E, is calculated from the curvature κ at the top support

$$E = \frac{M}{\kappa\, I_0} \qquad (2)$$

where I_0 is the inertia moment of the cross-section, M the bending moment at the load application point.

The derivative of the curvature, which is piece-wise constant, is proportional to forces on the two lower supports. From this information and global equilibrium of the beam, the bending moment is computed as a function of the applied load. The maximum stress calculated at the bottom face of the beam is shown as a function of the longitudinal

strain in Figure 12, with the points used for assessing the Young's modulus highlighted between cyan circles. Such points were chosen to avoid the beginning of the test, where small displacements and accommodation of the setup took place and also the steps close to the peak load where it deviated from linearity (due to multiple crack initiations and propagation, see Figure 11(c,d)). With such approach, the Young's modulus calculated from the images obtained for the front surface is equal to 8.4 GPa, while it is equal to 8.5 GPa with the data from the opposite surface.

For this same material, but sintered at 1450°C, a value of 17 GPa was obtained when using cohesive elements to simulate a WST experiment performed at room temperature inside a tomograph[47]. Tests using the impulse excitation technique showed that samples sintered at 1400°C may present a dynamic Young's modulus up to 20% lower than those sintered at 1450°C. Moreover, some thermal cycles performed to check that the applied pattern may also have damaged the specimen and further reduced the Young's modulus. It is worth reminding that the experiments reported herein aim to illustrate the methodological procedures, and
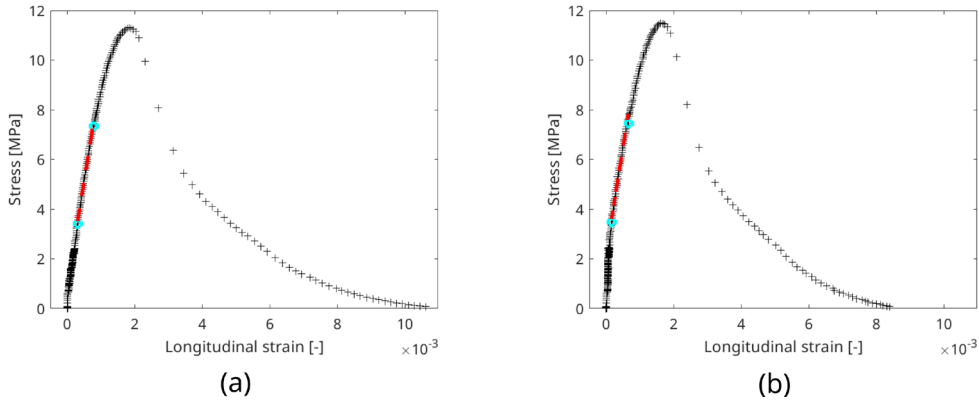
Figure 12. Maximum stress (*i.e.,* at the bottom of the beam) as the respective longitudinal strain for the (a) front and (b) back analyzed surfaces. The cyan circles depict the points used for calculating the Young's modulus (the same points are highlighted in Figure 10(b)), and the respective affine slope is shown as a dashed red line.
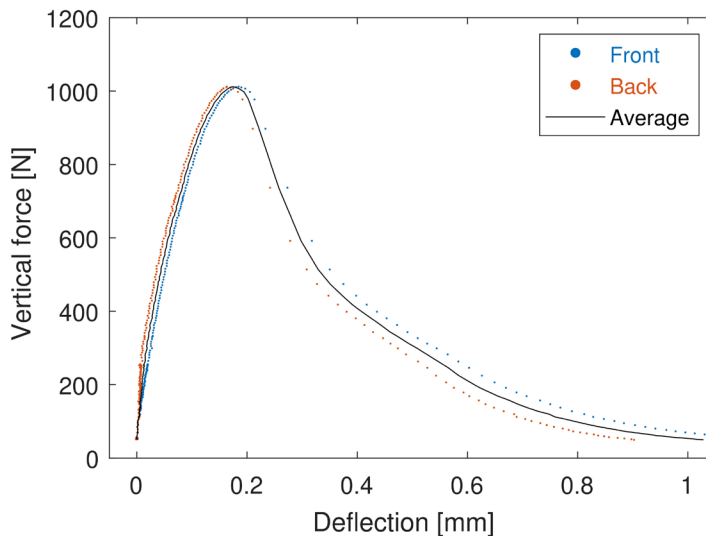

Figure 13. Vertical force as a function of the deflection (which is significantly different from the actuator displacement, see Figure 10(b)) calculated on the front and back surfaces, as well as the average among them, for the three-point bend test.

the variability of such results among several samples will be (one of) the focus of future investigations. The maximum flexural stress in this unnotched sample is of the order of 11.5 MPa, which is about 3.3 times the cohesive strength calibrated for WST of the same material and sintering temperature (but tested at 600°C), and 1.8 times the notch tensile stress[47].

From the degrees of freedom of the reduced kinematics, a direct result is the beam deflection, by taking the vertical displacement of the middle node and removing the average vertical displacement from both outer nodes. The loading curves as a function of such deflections are displayed in Figure 13, with a deflection at the peak load about 15% of the actuator displacement for the ultimate load reported in Figure 10(b), highlighting the importance of measuring the displacement directly on the sample. Moreover, misalignment and accommodation may occur at the beginning of the experiment in such setup, as observed below 300 N in Figure 13, whose effect is mitigated when the average is considered. By integrating the curves from

Figure 13, the work of fracture is obtained, which allows for the calculation of the fracture energy by dividing it by twice the cross-section area since two new surfaces are created. In the present case, fracture energies of 280 J/m², 246 J/m², and 263 J/m² are obtained for the front, back, and average among both surfaces, respectively. Such levels can be compared to 227 J/m², the fracture energy estimated in Ref.[50] from the raw loading curve (deemed to be an upper bound) for a WST performed at 600°C on a sample with similar heat treatment as herein. Even if differences may arise from other geometries, this result indicates that the required energy to propagate a crack tends to increase with the testing temperature for this material, from room temperature to 600°C[51] and from 600°C to 900°C. The aforementioned estimate of the Young's modulus is confirmed by using the slope (for the same time steps highlighted in Figure 12) of the load vs. deflection curves (Figure 13), which results in a level of 9.1 GPa.

Another advantage of using full-field measurements in such tests is the possibility to better visualize initiation and
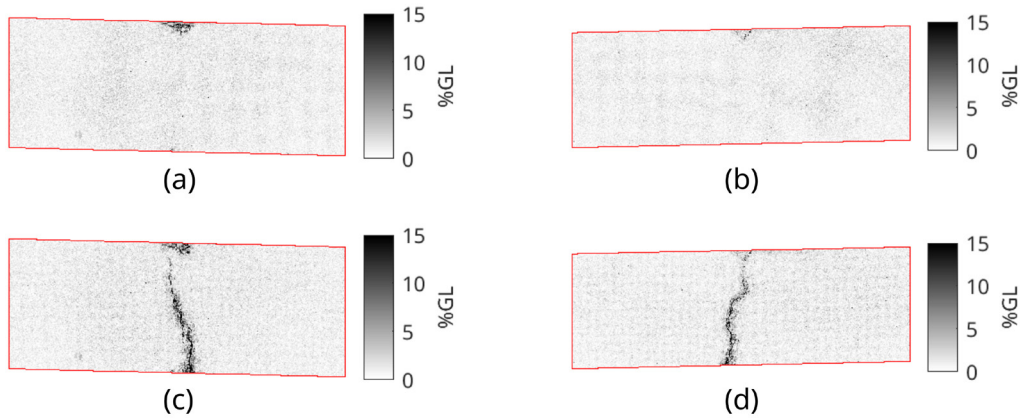
Figure 14. Absolute gray level residuals normalized by the dynamic range of the reference images for (a, b) the ultimate load and for (c,d) the last frame. Results for the front surface in sub-figures (a,c) and for the back surface in sub-figures (b,d).

propagation of cracks. For instance, in the displacement fields shown in Figure 11(c,d), zones with very high displacement gradients are observed in the bottom part, but the crack opening was still too small to be captured in gray level residuals normalized by the dynamic range, see Figure 14(a,b). This observation indicates that the opening of the cracks seen in the displacement is less than or very close to the physical size of one pixel (*i.e.,* 14.8 μm). However, only one of them further propagated forming the major crack, as seen in the final absolute gray level residuals shown in Figure 14(c,d). A slight curvature is seen, which looks horizontally mirrored when both faces are compared, since it is observed from opposite sides.
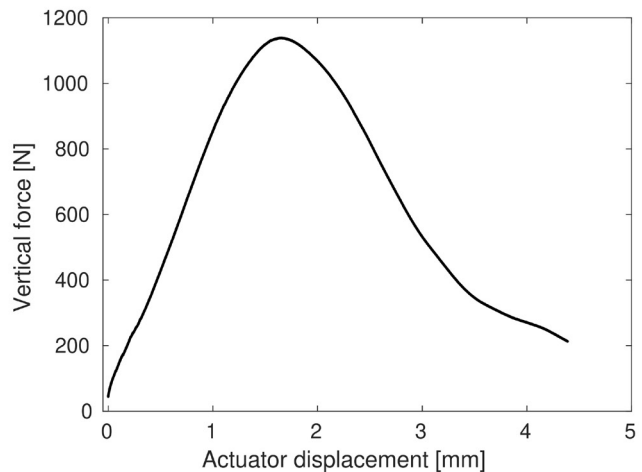
3.3. Wedge splitting test

The WST sample was made with the same material and using the same processing as that of the TPB specimen, with the only difference coming from the sintering temperature of 1450°C, which was shown to considerably change the fracture energy[50,51]. A similar protocol to that described for the TPB

experiment was followed for the WST, whose setup inside the furnace is displayed in Figure 15(a). However, a dwell of 2.5 h was applied after reaching 900°C to thermally stabilize the sample before starting the mechanical loading, and the test was stopped post-peak at 20% of the ultimate load. From heating and, consequently, thermal expansion of the setup, about 3 mm in actuator displacement was required to maintain the pre-load during this first stage. In this test, a stabler crack propagation was achieved compared with the bend test (Figure 15(b)).

For this case, two different meshes were used and shown along with the reference images acquired at 900°C in Figure 16(a,b). Since the sample could not be fully visualized, it is displayed in a blue contour to improve the understanding. The applied pattern is seen as darker speckles on the sample surface, along with brighter regions indicating the focus of the four lighting LEDs. The first mesh (in red, with a mean element size of 0.9 mm or 80 px) encompassed most of the illuminated area for measurig the overall kinematics, as exemplified by the horizontal displacements shown in Figure 16(c,d) for the time step corresponding to the ultimate
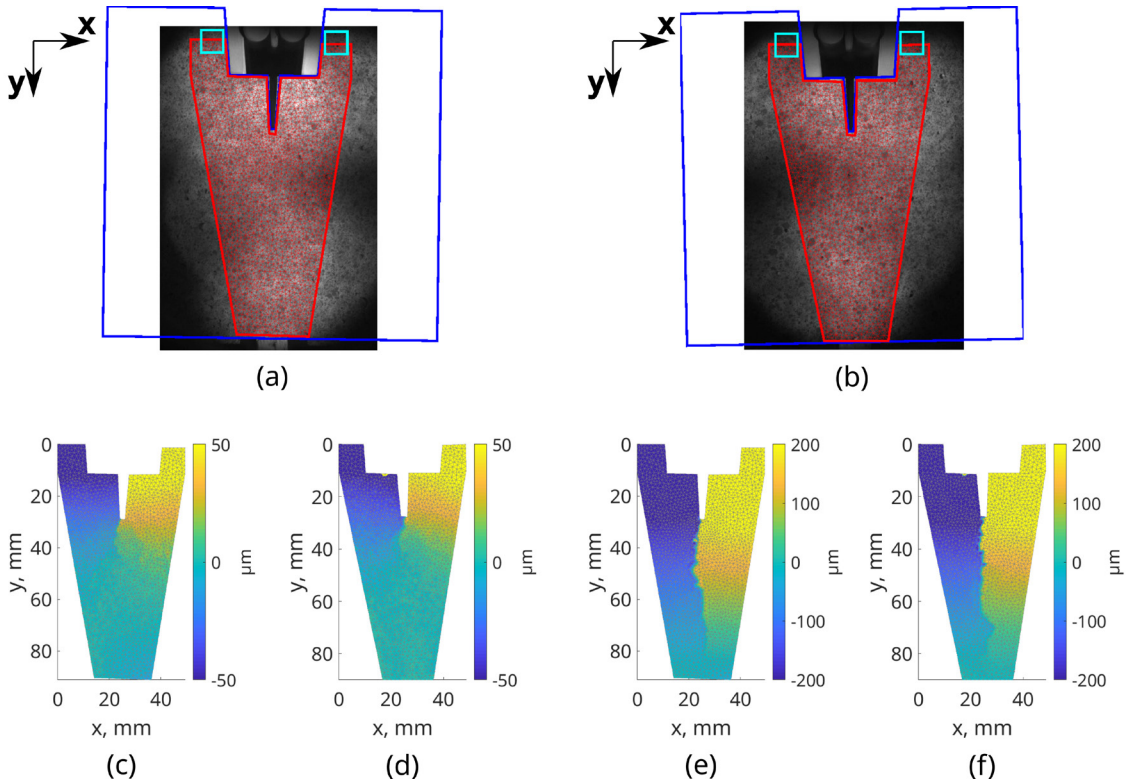

Figure 15. (a) *Post-mortem* wedge splitting test sample inside the F900 furnace. (b) Loading curve obtained with the 900°C setup.

Figure 16. (a,b) Reference images with two sets of meshes used for analyzing the WST performed at 900°C. The blue contour delineates the specimen, while the red one depicts the mesh used for analyzing the chosen region on both sides. Zones used to calculate the CMOD are depicted with cyan boxes. Horizontal displacement fields for (c,d) the step of the ultimate force and (e,f) the last time step. Results for the front surface in sub-figures (a,c,e) and for the back surface in sub-figures (b,d,f). 1 px ≈ 11.4 µm.

force. For this mesh, the standard displacement uncertainties (Appendix A) were equal to 9 cpx (*i.e.,* ≈ 1 µm). An opening trend is seen at the top part, as expected, where the maximum displacement amplitudes are of the same order of magnitude as for the bend test (50 µm). Along the crack path, the displacements are considerably smaller. The second mesh (cyan boxes in Figure 16(a,b)) depicts the mid-height of the surfaces where the loading was applied, whose displacements are utilized for calculating the so-called Crack Mouth Opening Displacement (CMOD). For this second mesh, although elements about five times bigger were used (*i.e.,* only four nodes for each cyan box in Figure 16(a,b), the standard displacement uncertainty was higher, *i.e.,* 13 cpx (or 1.5 µm), which is related to the shadows on the top part that reduced the contrast in that region.

The splitting curves are displayed in Figure 17 by considering the splitting forces (*i.e.,* 5.715 times the vertical forces in the present configuration) as functions of the CMOD. The integration of these curves gives direct access to the work of fracture, after being divided by twice the ligament area. Even if a small difference is seen with the CMODs, one crack being more open for the first stage of the experiment, the resulting fracture energies are very similar, namely, 261 J/m² for the front face and 255 J/m² for the back face. These values are close to those reported for the three-point bend test, but the present test was stopped at 20% of the peak force. Therefore, it would result in a higher fracture energy if it was carried on. If a similar calculation
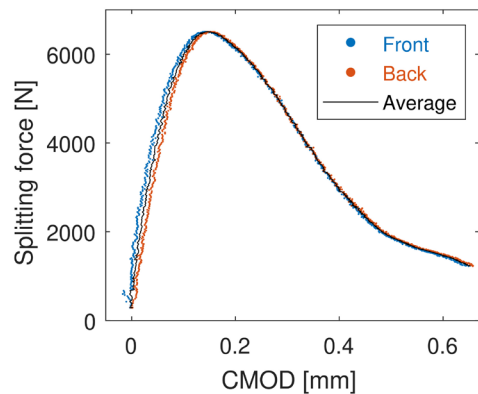
Figure 17. Horizontal loading curves for the Wedge Splitting Test (WST) performed at 900°C with the CMODs measured for both opposite surfaces.

is made but also considering the work performed by the testing machine (by integrating the curve in Figure 15(b)), a fracture energy of 301 J/m² is obtained, which is 15% higher, since it considers the deformation of the whole testing setup. It is worth noting that in Ref.[50], similar samples were tested at room temperature (presenting lateral grooves in the geometry to guide the crack) and 600°C, and levels of 143 J/m² and 264 J/m², respectively, were obtained from the work including the testing machine. These comparisons
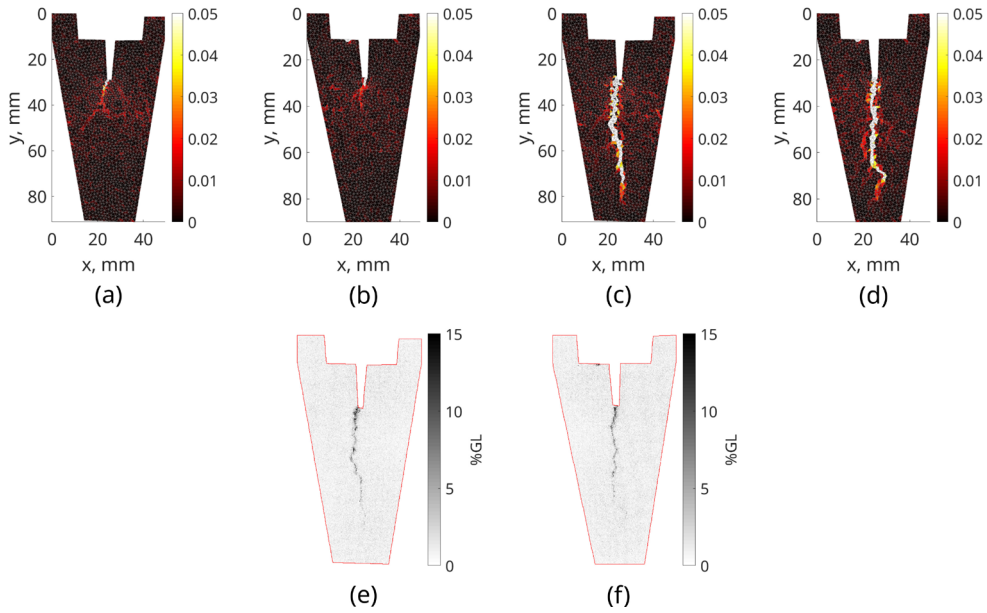
Figure 18. Maximum principal strains for (a,b) the time step of the ultimate force and (c,d) for the last time step of the WST performed at 900°C. (e,f) Absolute gray level residuals for the last analyzed time step normalized by the dynamic range of the reference images. Results for the front surface in sub-figures (a,c,e) and for the back surface in sub-figures (b,d,f).

further corroborate the levels discussed for the three-point bend test, indicating that the fracture energy tends to increase with the temperature up to 900°C.

To visualize the cracks, the maximum principal strain, whose standard uncertainty was 9×10^{-4}, is reported. The advantage of this procedure is to highlight cracks in all directions. For instance, these fields, for the same time step of the ultimate force discussed in Figure 16(c,d), are displayed in Figure 18(a,b). At this stage, the crack propagated more on the front side, while also presenting some small branches. Moreover, it initiated on the left side of the notch on the front surface, while on the back surface it initiated closer to the middle of the notch. Another result from DIC analyses is the gray level residual map, in which their absolute value for the last analyzed frame is shown in Figure 18 for both analyzed surfaces. The overall crack path is easily visible on both sides, although more hypotheses (*i.e.,* choice of a model) are needed to properly define the crack tip[37]. For the present case, no significant crack branching was seen, and the crack propagated on a quasi-straight path. Such trends may allow for the assumption of a straight crack path when using these data for parameter calibration purposes.

4. Conclusion and Perspectives

The design of a setup suitable for thermomechanical experiments up to 900°C assisted by DIC was presented with discussions aiming to help the reader interested in building a similar equipment. Thanks to six windows, the visualization and illumination of sample surfaces from different angles is possible. Such setup aims to enable for the measurement of full-field displacements at high temperatures, in environments similar to service conditions of many materials represented here by refractories. This type of experiment can be used in the calibration and validation of material parameters for numerical simulations. Three possibilities of usage were exemplified. The first one consisted of a dilatometry test, whose full-fields may help to quantify thermal expansion of bigger specimens than usual procedures (*e.g.,* for compositions with big aggregates) and also investigate localized phenomena such as thermally induced phase transformations and/or cracks. The second and third examples had mechanical loadings. The second one was a three-point bend test, which allowed for the quantification of the Young's modulus, the ultimate strength, and the fracture energy of the material. The third was a wedge splitting test, mostly used for measuring the fracture energy of brittle materials. In both cases, the displacement measured directly on sample surfaces (using DIC) was crucial for such measurements. DIC was also used to illustrate the possibility of investigating crack propagation on opposite surfaces of the samples.

In the future, more experiments will be conducted to analyze the variability of results. Numerical simulations of such experiments will also be used for testing suitable constitutive models for thermomechanical loadings, which will be analyzed using the gathered full-field data. Thermal expansion, crack propagation, and sintering processes are the three main axes of investigation foreseen using this setup. Last, a similar setup suitable for higher temperatures is being designed, allowing for yet a bigger range of thermomechanical conditions.

5. Acknowledgments

6. References

1. Rao YS, Shivamurthy B, Shetty N, Mohan NS. Thermomechanical properties of carbon fabric reinforced epoxy laminates with h-BN and MoS$_2$ fillers. Mater Res. 2021;24(6):e20210215. http://doi.org/10.1590/1980-5373-mr-2021-0215.

2. Sciuti VF, Melo CC, Canto LB, Canto RB. Influence of surface crystalline structures on DSC analysis of PTFE. Mater Res. 2017;20(5):1350-9. http://doi.org/10.1590/1980-5373-mr-2017-0326.

3. Vasconcelos GC, Mazur RL, Ribeiro B, Botelho EC, Costa ML. Evaluation of decomposition kinetics of poly (ether-ether-ketone) by thermogravimetric analysis. Mater Res. 2014;17(1):227-35. http://doi.org/10.1590/S1516-14392013005000202.

4. Zhang X, Chen Y, Hu J. Recent advances in the development of aerospace materials. Prog Aerosp Sci. 2018;97:22-34. http://doi.org/10.1016/j.paerosci.2018.01.001.

5. Murty KL, Charit I. Structural materials for Gen-IV nuclear reactors: challenges and opportunities. J Nucl Mater. 2008;383(1-2):189-95. http://doi.org/10.1016/j.jnucmat.2008.08.044.

6. Lee WE, Gilbert M, Murphy ST, Grimes RW. Opportunities for advanced ceramics and composites in the nuclear sector. J Am Ceram Soc. 2013;96(7):2005-30. http://doi.org/10.1111/jace.12406.

7. Wang X, Gao X, Zhang Z, Cheng L, Ma H, Yang W. Advances in modifications and high-temperature applications of silicon carbide ceramic matrix composites in aerospace: a focused review. J Eur Ceram Soc. 2021;41(9):4671-88. http://doi.org/10.1016/j.jeurceramsoc.2021.03.051.

8. Tessier-Doyen N, Glandus JC, Huger M. Untypical Young's modulus evolution of model refractories at high temperature. J Eur Ceram Soc. 2006;26(3):289-95. http://doi.org/10.1016/j.jeurceramsoc.2004.10.028.

9. Schiavon FL, Zanardi H, Zago IP, Angélico RA. Prediction of elastic parameters of particle reinforced composites using finite element simulations. Mater Res. 2023;26:e20220475. http://doi.org/10.1590/1980-5373-mr-2022-0475.

10. Poirier J, Blond E, Bilbao E, Michel R, Coulon A, Gillibert J, et al. New advances in the laboratory characterization of refractories: testing and modelling. Metall Res Technol. 2017;114(6):610. http://doi.org/10.1051/metal/2017068.

11. Lyons JS, Liu J, Sutton MA. High-temperature deformation measurements using digital-image correlation. Exp Mech. 1996;36(1):64-70. http://doi.org/10.1007/BF02328699.

12. Sutton MA, Orteu JJ, Schreier H. Image correlation for shape, motion and deformation measurements: basic concepts, theory and applications. New York: Springer Science & Business Media; 2009. http://doi.org/10.1007/978-0-387-78747-3.

13. Sutton MA. Computer vision-based, noncontacting deformation measurements in mechanics: a generational transformation. Appl Mech Rev. 2013;65(5):050802. http://doi.org/10.1115/1.4024984.

14. Mathieu F, Leclerc H, Hild F, Roux S. Estimation of elastoplastic parameters via weighted FEMU and integrated-DIC. Exp Mech. 2015;55(1):105-19. http://doi.org/10.1007/s11340-014-9888-9.

15. Neggers J, Mathieu F, Hild F, Roux S, Swiergiel N. Improving full-field identification using progressive model enrichments. Int J Solids Struct. 2017;118:213-23. http://doi.org/10.1016/j.ijsolstr.2017.03.013.

16. Neggers J, Mathieu F, Hild F, Roux S. Simultaneous full-field multi-experiment identification. Mech Mater. 2019;133:71-84. http://doi.org/10.1016/j.mechmat.2019.03.001.

17. Roux S, Hild F. Optimal procedure for the identification of constitutive parameters from experimentally measured displacement fields. Int J Solids Struct. 2020;184:14-23. http://doi.org/10.1016/j.ijsolstr.2018.11.008.

18. Pierron F, Grédiac M. Towards Material Testing 2.0: a review of test design for identification of constitutive parameters from full-field measurements. Strain. 2021;57(1):e12370. http://doi.org/10.1111/str.12370.

19. Pierron F. Material Testing 2.0: a brief review. Strain. 2023;59(3):e12434. http://doi.org/10.1111/str.12434.

20. Sova RM, Linevsky MJ, Thomas ME, Mark FF. High-temperature optical properties of oxide ceramics. Johns Hopkins APL Tech Dig. 1992;13(3):368-78.

21. Berny M, Archer T, Mavel A, Beauchêne P, Roux S, Hild F. On the analysis of heat haze effects with spacetime DIC. Opt Lasers Eng. 2018;111:135-53. http://doi.org/10.1016/j.optlaseng.2018.06.004.

22. Archer T, Beauchêne P, Huchette C, Hild F. Global digital image correlation up to very high temperatures with grey level corrections. Meas Sci Technol. 2019;31(2):024003. http://doi.org/10.1088/1361-6501/ab461e.

23. Vargas R, Canto RB, Hild F, Roux S. On accounting for speckle extinction via DIC and PCA. Opt Lasers Eng. 2022;149:106813. http://doi.org/10.1016/j.optlaseng.2021.106813.

24. Appleby MP, Zhu D, Morscher GN. Mechanical properties and real-time damage evaluations of environmental barrier coated SiC/SiC CMCs subjected to tensile loading under thermal gradients. Surf Coat Tech. 2015;284:318-26. http://doi.org/10.1016/j.surfcoat.2015.07.042.

25. Christian WJR, Dvurecenska K, Amjad K, Pierce J, Przybyla C, Patterson EA. Real-time quantification of damage in structural materials during mechanical testing. R Soc Open Sci. 2020;7(3):191407. http://doi.org/10.1098/rsos.191407.

26. Niu G, Zhu R, Lei H, Zhang R, Wang P, Qu Z, et al. Internal damage evolution investigation of C/SiC composites using in-situ tensile X-ray computed tomography testing and digital volume correlation at 1000°C. Compos, Part A Appl Sci Manuf. 2022;163:107247. http://doi.org/10.1016/j.compositesa.2022.107247.

27. Forna-Kreutzer JP, Ell J, Barnard H, Pirzada TJ, Ritchie RO, Liu D. Full-field characterisation of oxideoxide ceramic-matrix composites using X-ray computed micro-tomography and digital volume correlation under load at high temperatures. Mater Des. 2021;208:109899. http://doi.org/10.1016/j.matdes.2021.109899.

28. Pirzada TJ, Liu D, Ell J, Barnard H, Sulák I, Galano M, et al. In situ observatioˇ of the deformation and fracture of an alumina-alumina ceramic-matrix composite at elevated temperature using x-ray computed tomography. J Eur Ceram Soc. 2021;41(7):4217-30. http://doi.org/10.1016/j.jeurceramsoc.2021.01.030.

29. Turpin L, Roux S, Bénézech J, Couégnat G, King A, Caty O, et al. Quantitative thermomechanical characterisation of 3D-woven SiC/SiC composites from in-situ tomographic and thermographic imaging. Compos Struct. 2023;307:116626. http://doi.org/10.1016/j.compstruct.2022.116626.

30. Yuan G, Forna-Kreutzer JP, Xu P, Gonderman S, Deck C, Olson L, et al. In situ high-temperature 3D imaging of the damage evolution in a SiC nuclear fuel cladding material. Mater Des. 2023;227:111784. http://doi.org/10.1016/j.matdes.2023.111784.

31. Liu C, Shi D, Guo Y, Cheng Z, Li Z, Yang X. Experimental and numerical study on creep behaviors of 2D twill woven quartz fiber/silica matrix composites. Ceram Int. 2021;47(24):34481-91. http://doi.org/10.1016/j.ceramint.2021.08.362.

32. Leplay P, Réthoré J, Meille S, Baietto MC. Identification of asymmetric constitutive laws at high temperature based on digital image correlation. J Eur Ceram Soc. 2012;32(15):3949-58. http://doi.org/10.1016/j.jeurceramsoc.2012.03.024.

33. Zhou ZP, Yuan WZ, Zhu W, Hu XP, Zou Y, Wu Q, et al. In situ measurements of the hightemperature mechanical properties of ZrO2-doped YTaO$_4$ ceramic by three-point bending combined with a digital image correlation method. Ceram Int. 2022;48(5):7159-67. http://doi.org/10.1016/j.ceramint.2021.11.277.

34. Gazeau C, Gillibert J, Blond E, Geffroy PM, Richet N. Experimental set up for the mechanical characterization of plane ITM membrane at high temperature. J Eur Ceram Soc. 2015;35(14):3853-61. http://doi.org/10.1016/j.jeurceramsoc.2015.06.026.

35. Kaczmarek R, Dupré JC, Doumalin P, Pop O, Teixeira L, Huger M. High-temperature digital image correlation techniques for full-field strain and crack length measurement on ceramics at 1200°C: optimization of speckle pattern and uncertainty assessment. Opt Lasers Eng. 2021;146:106716. http://doi.org/10.1016/j.optlaseng.2021.106716.

36. Doitrand A, Estevez R, Thibault M, Leplay P. Fracture and cohesive parameter identification of refractories by Digital Image Correlation up to 1200°C. Exp Mech. 2020;60(5):577-90. http://doi.org/10.1007/s11340-020-00584-7.

37. Vargas R, Neggers J, Canto RB, Rodrigues JA, Hild F. Analysis of wedge splitting test on refractory castable via integrated DIC. J Eur Ceram Soc. 2016;36(16):4309-17. http://doi.org/10.1016/j.jeurceramsoc.2016.07.007.

38. Vargas R, Neggers J, Canto RB, Rodrigues JA, Hild F. Analysis of a castable refractory using the wedge splitting test and cohesive zone model. J Eur Ceram Soc. 2019;39(13):3903-14. http://doi.org/10.1016/j.jeurceramsoc.2019.03.009.

39. Sutton M, Yan J, Tiwari V, Schreier H, Orteu J. The effect of out-of-plane motion on 2d and 3d digital image correlation measurements. Opt Lasers Eng. 2008;46(10):746-57. http://doi.org/10.1016/j.optlaseng.2008.05.005.

40. Pierré J-E, Passieux J-C, Périé J-N. Finite element stereo digital image correlation: framework and mechanical regularization. Exp Mech. 2017;57(3):443-56. http://doi.org/10.1007/s11340-016-0246-y.

41. Hild F, Roux S. Digital image correlation. Weinheim: Wiley-VCH; 2012. p. 183-228.

42. Leplay P, Lafforgue O, Hild F. Analysis of asymmetrical creep of a ceramic at 1350°C by Digital Image Correlation. J Am Ceram Soc. 2015;98(7):2240-7. http://doi.org/10.1111/jace.13601.

43. Hayashi H, Saitou T, Maruyama N, Inaba H, Kawamura K, Mori M. Thermal expansion coefficient of yttria stabilized zirconia for various yttria contents. Solid State Ion. 2005;176(5-6):613-9. http://doi.org/10.1016/j.ssi.2004.08.021.

44. Kulczyk-Malecka J, Zhang X, Carr J, Nozahic F, Estournès C, Monceau D, et al. Thermo-mechanical properties of SPS produced self-healing thermal barrier coatings containing pure and alloyed MoSi$_2$ particles. J Eur Ceram Soc. 2018;38(12):4268-75. http://doi.org/10.1016/j.jeurceramsoc.2018.04.053.

45. Dey T, Das Sharma A, Dutta A, Basu RN. Transition metal-doped yttria stabilized zirconia for low temperature processing of planar anode-supported solid oxide fuel cell. J Alloys Compd. 2014;604:151-6. http://doi.org/10.1016/j.jallcom.2014.03.056.

46. Vargas R, Canto RB, Hild F. Fracture energy evaluation of refractories in wedge splitting tests from notch opening displacements. J Eur Ceram Soc. 2021;41(10):5367-79. http://doi.org/10.1016/j.jeurceramsoc.2021.02.055.

47. Vargas R, Canto RB, Smaniotto B, Hild F. Calibration of cohesive parameters for a castable refractory using 4D tomographic data and realistic crack path from in-situ wedge splitting test. J Eur Ceram Soc. 2023;43(2):676-91. http://doi.org/10.1016/j.jeurceramsoc.2022.09.040.

48. Hild F, Roux S, Gras R, Guerrero N, Marante ME, Flórez-López J. Displacement measurement technique for beam kinematics. Opt Lasers Eng. 2009;47(3):495-503. http://doi.org/10.1016/j.optlaseng.2008.03.006.

49. Hild F, Roux S. Digital image correlation: from displacement measurement to identification of elastic properties: a review. Strain. 2006;42(2):69-80. http://doi.org/10.1111/j.1475-1305.2006.00258.x.

50. Vargas R, Pinelli X, Smaniotto B, Hild F, Canto RB. On the effect of sintering temperature on fracture energy of Alumina-Mullite-Zirconia castable at 600°C. J Eur Ceram Soc. 2021;41(7):4406-18. http://doi.org/10.1016/j.jeurceramsoc.2021.01.023.

51. Vargas R, Canto RB, Hild F. Cohesive properties of refractory castable at 600°C: effect of sintering and testing temperature. J Eur Ceram Soc. 2022;42(14):6733-49. http://doi.org/10.1016/j.jeurceramsoc.2022.06.070.

Supplementary material

The following online material is available for this article:

Appendix A - DIC hardware parameters and uncertainties.

Appendix B - Validation experiments.